33rd Annual International Conference of the IEEE EMBS
Boston, Massachusetts USA, August 30 - September 3, 2011

Automated lymph node detection and classification on breast and prostate cancer SPECT-CT images

Laszlo Papp, Norbert Zsoter, Charlotte Loh, Baeumer Ole, Bernhard Egeler, Ildiko Garai, Ulf Luetzen

***Abstract*— We present a novel detection and classification method to process SPECT-CT images representing breast and prostate lymph nodes. Lymph nodes are those nodes that are near the primer tumor and may become cancerous in time, hence their early detection is a key factor for the successful treatment of the patient. Prior methods focus on the visual aid to manually detect the lymph nodes which still makes the process time-consuming. Other solutions segment the lymph nodes only on CT, where the small lymph nodes may not be located accurately. Our solution processed both SPECT and CT data to provide an accurate classification of all SPECT hot spots. The method has been validated on a huge amount of medical data. Results show that our method is a very effective tool to support physicians working with related images in the field of nuclear medicine.**

I. INTRODUCTION

Individuals suffering from prostate or breast cancer are generally involved in Sentinel Lymph Node (SLN) examinations that are common procedures in nuclear medicine [1], [2], [3]. Lymph nodes are near the primer tumor and may become cancerous in time even after treating the primer one [1], [2]. That particular lymph node which is located near the primer tumor - generally having the highest uptake - is called the sentinel lymph node [7]. The SLN has the highest probability to become cancerous in time, therefore the early detection and invasive SLN removal is a key step for the successful treatment of the patient. To visualize the lymph nodes, radioactive activity is injected directly into the primer tumor, then a SPECT-CT (Single Photon Emission Computed Tomography - Computed Tomography) hybrid scan is acquired [1]. The common way of interpretation is the visual analysis of the SPECT-CT images performed by nuclear medicine specialists [2], [5]. The SPECT-CT data analysis depends solely on the examiner's experience and is very time-consuming [6]. The nature of the SPECT image makes it difficult to automate the lymph node segmentation. Lymph nodes normally have only 1-2% uptake of the total injected activity [2], [6]. The part of the activity may go into the kidneys, liver and also into bones (see Fig. 1).

Although several SLN segmentation methods have been proposed, most of them are semi-automated and still require the presence of an experienced physician [7], [8], or operate on CT images where only far-gone staged lymph nodes can be detected [9], [10]. On the other hand prior methods focus on detecting only the SLN, and they do not support the tracking of all lymph node changes in long periods.

Due to the above reasons our goal was to design a fully automated post-processing method which detects and classifies all lymph nodes on SPECT-CT studies built on current professional physician knowledge. We especially focused on achieving the minimal ratio of the false negative classifications, since this factor was the most important one to make our method acceptable in the daily routine. For the hot spot detection and classification both SPECT and CT data were processed. Several indices were collected for all hot spots. These indices were the base of a classification performed on the collected clinical data.

II. MATERIALS AND METHODS

A. Patient data

For prostate and breast lymph node examples 74 and 71 anonymous patient data was collected respectively. The data included the SPECT-CT reconstructed image pairs in standard DICOM format and the corresponding medical report providing detailed information about the manually detected lymph nodes. The SPECT-CT data was acquired 0.5-2 hours after administering 30-150 MBq ^{99m}Tc-Nanocolloid. The CT images had $1.0 \times 1.0 \times 5.0$mm voxel size with 512×512 axial resolution. The SPECT images had 4.0mm uniform voxel size with 128×128 axial resolution. The units of the voxel values were *Cts* (Counts) and *HU* (Hounsfield) for the SPECT and the CT respectively.

B. Methods

The whole process included three main steps: SPECT hot spot detection, CT tissue segmentation and the classification to determine for all hot spots whether they are true of false findings.

1) SPECT hot spot segmentation: Since SPECT images had poor spatial resolution, they were resampled to $1.0 \times 1.0 \times 1.0$mm voxel size by a 3D cubic b-spline interpolation [11]. The result of the resampling was stored in I_{sp} image. According to initial trials, values less than $T_{bck} = 0.001 \cdot max(I_{sp})$ were associated with background noise, hence these values were eliminated by (1).

$$\forall \overline{x} \in C^{I_{sp}} : I_{sp}(\overline{x}) = \max\left(I_{sp}(\overline{x}), T_{bck}\right) \qquad (1)$$

where $C^{I_{sp}} \subseteq \mathbb{N}^3$ denotes the valid voxel coordinates $\overline{x}$ of image I_{sp}, $I_{sp}(\overline{x})$ denotes the voxel value in I_{sp} image at $\overline{x}$ voxel coordinate and $\overline{x} \in \mathbb{N}^3$.

L. Papp and N. Zsoter are with Mediso Medical Imaging Systems Ltd., Baross str. 91-95, Budapest, Hungary laszlo.papp@mediso.hu
C. Loh, B. Ole, B. Egeler and U. Luetzen are with Medical University of Kiel, Germany uluetzen@nuc-med.uni-kiel.de
I. Garai is with Medical University of Debrecen, Scanomed Ltd., Hungary garai@belklinika.com

Our method built on the fact that lymph nodes always have a local maxima (high peak) typically in their geometrical center. The detection of these high peak positions was the first step to segment all hot spots from SPECT images. High peak positions were detected by a 3×3×3 voxel mask around all voxels inside of image I_{sp} and collected to $LM \subseteq \mathbb{N}^3$ coordinate set as defined by (2).

$$\begin{aligned} &\forall \overline{p} \in C^{I_{sp}} : LM \cup \overline{p}| \\ &I_{sp}(\overline{p}) = \max_{\overline{k} \in D_3(\overline{p})} \left(I_{sp}(\overline{k})\right)) \end{aligned} \tag{2}$$

Assuming that $\overline{p} = (p_1, p_2, p_3)$, $D_3(\overline{p})$ is defined as (3).

$$\begin{aligned} D_a(p_1, p_2, p_3) = \big\{(i,j,k) \in \mathbb{N}^3 | \\ p_1 - \left\lfloor \frac{a}{2} \right\rfloor \leq i \leq p_1 + \left\lfloor \frac{a}{2} \right\rfloor , \\ p_2 - \left\lfloor \frac{a}{2} \right\rfloor \leq j \leq p_2 + \left\lfloor \frac{a}{2} \right\rfloor , \\ p_3 - \left\lfloor \frac{a}{2} \right\rfloor \leq k \leq p_3 + \left\lfloor \frac{a}{2} \right\rfloor \big\} \end{aligned} \tag{3}$$

where $a \in \mathbb{N}$ defined the kernel size.

Since it was possible that in a region more local maxima positions were direct neighbors, the LM set had to be filtered in order to keep only one peak position for all regions. The filtering was performed by checking whether any direct neighbor of all $\overline{p} \in LM$ was located in LM as defined by (4).

$$\forall \overline{p} \in LM : LM \backslash \overline{p} \; if \; D_3(\overline{p}) \in LM \tag{4}$$

Having the voxel coordinates of all peak positions in I_{sp}, a recursive region growing was performed from all $\overline{p} \in LM$ points as defined by the hot spot segmentation algorithm detailed in Tab. I.

The region growing started from a $\overline{p} \in LM$ peak position and recursively collected those neighboring coordinates whose value was monotone decreasing in I_{sp}. All regions of a $\overline{p} \in LM$ peak position was associated with a unique ID in an I^s_{sp} image which had the same size/voxel characteristics as I_{sp} image had. If a region growing involved an already processed coordinate, then its corresponding I^s_{sp} value ID was changed to -1 which meant that the coordinate was the part of another region as well. Later on these common regions were eliminated from I^s_{sp} image by (5)

$$\forall \overline{x} \in C^{I_{sp}} | I^s_{sp}(\overline{x}) = -1 : I^s_{sp}(\overline{x}) = 0 \tag{5}$$

The result of the SPECT segmentation was the I^s_{sp} image representing ID different hot spot regions labeled with unique values, and the background region which was associated with value 0 (see Fig. 1).

2) CT tissue segmentation: The CT image was resampled to 1.0 × 1.0 × 1.0mm voxel size by a 3D cubic b-spline interpolation [11] in order to provide an I_{ct} image having the same resolution as I_{sp} had. Assuming that $C^{I_{ct}} \subseteq \mathbb{N}^3$ denoted the valid voxel coordinates inside of image I_{ct}, the common valid coordinates were denoted as $C^{I_{sp}, I_{ct}} = C^{I_{ct}} \cap C^{I_{sp}}$.

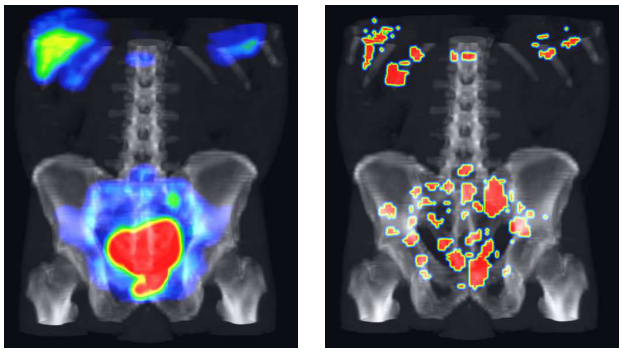

Fig. 1. Left: Coronal view of a SPECT-CT lymph node image representing several hot spots over the injection region, in kidneys, bones and liver as well. Right: The result of the SPECT hot spot detection step (I^s_{sp}) fused together with the original CT.

Based on the above $C^{I_{sp}, I_{ct}}$ set, a I^s_{ct} image was created representing 4 different values associated to air, fat, muscle and bone as defined by (6).

$$\forall \overline{x} \in C^{I_{sp}, I_{ct}} : I^s_{ct}(\overline{x}) = LUT_{ct}\left(I_{ct}(\overline{x})\right) \tag{6}$$

where $LUT_{ct}(v)$ denoted a lookup table definition for Hounsfield value $v \in \mathbb{Z}$ as defined by (7). The lookup table values were based on the standard Hounsfield Scale [12] fine-tuned by observation performed on five of our collected CT images.

$$LUT_{ct}(v) = \begin{cases} 0 & \text{if} \quad & v & < -200 \\ 1 & \text{if} \quad -200 \leq & v & < -20 \\ 2 & \text{if} \quad -20 \leq & v & < 150 \\ 3 & \text{if} \quad & v & \geq 150 \end{cases} \tag{7}$$

Where v and all numeric values are Hounsfield values [12].

Hounsfield values of bones were located on a wide range of the standard Hounsfield Scale [12], hence it was difficult to correctly associate the spongy tissue located inside of surrounding compact bones. Therefore spongy tissues were often assigned to air-fat-muscle regions based on the above lookup table definition. In order to correct these wrong assignments, the spongy regions were filled-up by morphological operations over the axial slices of I^s_{ct} as presented in [13]. The result of the post-processed CT tissue segmentation was stored in I^s_{ct} image (see Fig. 2).

3) Classification: The first step of the classification was the identification of all disjunctive hot spots located on I^s_{sp} image. The location was performed by storing the voxel coordinates of all $1 \leq i \leq ID$ regions into their corresponding $H_i \subseteq \mathbb{N}^3$ coordinate set as defined by (8). The hot spot coordinate sets were stored in $H = \{H_1, \ldots, H_{ID}\}$ set. The goal of the classification was to determine two sets $HT \subseteq \mathbb{N}$ and $HF \subseteq \mathbb{N}$ denoting the set of true and false findings respectively, where $i \in HT$ and $j \in HF$ meant that H_i and H_j hot spots were true and false findings respectively.

TABLE I

ALGORITHM OF THE SPECT HOT SPOT SEGMENTATION

1	$ID = 0$	Initialize $ID \in \mathbb{N}$ value
2	$\forall \overline{p} \in LM$:	process all coordinates in LM
3	$ID = ID + 1$	increment ID value
4	$(x, y, z) = \overline{p}$	read the coordinates of $\overline{p}$
5	$LM \backslash \overline{p}$	exclude the read $\overline{p}$ coordinate from LM
6	if $I^s_{sp}(x, y, z) \neq -1$:	if the coordinate is not a common one...
7	$I^s_{sp}(x, y, z) = ID$	associate it with the actual ID value in I^s_{sp}
8	$\forall (i, j, k) \in D_3(x, y, z) \vert (i, j, k) \in C^{I_{sp}}$:	process all existing neighbors of (x, y, z)
9	if $I^s_{sp}(i, j, k) \neq ID$:	if the neighbor is not in current region...
10	if $I_{sp}(i, j, k) \leq I_{sp}(x, y, z)$:	if the neighbor has a monotone decreasing value...
11	if $I^s_{sp}(i, j, k) = 0$:	if the neighbor has not been processed by another region growing...
12	$LM \cup (i, j, k)$	store (i, j, k) coordinate to LM
13	else if $I^s_{sp}(i, j, k) > 0$:	else if the neighbor has been already signed by another region...
14	$I^s_{sp}(i, j, k) = -1$	sign the value of (i, j, k) coordinate as a common one
15	$LM \cup (i, j, k)$	store (i, j, k) coordinate to LM

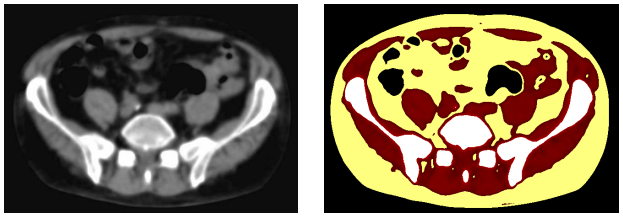

Fig. 2. Left: Axial view of an original CT image. Right: The tissue segmented (I^s_{ct}) image where air, fat, muscle and bone regions are colored by black, yellow, red and white respectively.

$$\forall \overline{x} \in C^{I_{sp}} : H_i \cup \overline{x} | I^s_{sp}(\overline{x}) = i \tag{8}$$

where $i > 0$, since the background values were not stored in H set.

Due to the way of administering the activity into the primer tumor, more hot spots may have belonged to the injection region. These hot spots were very close to one another and had the greatest uptake. Hot spots associated with the injection region had to be identified for two reasons: they were classified as false findings by default, and they were needed for further classification calculations. The identification step built on the fact that the injection region had extremely high activity comparing to the lymph nodes [7], [2]. The identification was based on (9).

$$\forall 1 \leq i \leq ID : H \backslash H_i, HF \cup i |$$
$$\max_{\overline{x} \in H_i} (I_{sp}(\overline{x})) > \sum_{j=1}^{ID} \frac{\max_{\overline{y} \in H_j} (I_{sp}(\overline{y}))}{ID} \tag{9}$$

Having the injection region hot spots classified as false findings, the coordinate $\overline{m} \in \mathbb{N}^3$ of their maximum I_{sp} value was detected based on (10).

$$\overline{m} = \underset{\overline{x} \in H_i | H_i \in HF}{\operatorname{argmax}} (I_{sp}(\overline{x})) \tag{10}$$

TABLE II

CLASSIFICATION INDICES CALCULATED FOR HOT SPOTS

Index	Calculation	Explanation
max_i	$\max_{\overline{x} \in H_i} (I_{sp}(\overline{x}))$	Maximum value in I_{sp}
min_i	$\min_{\overline{x} \in H_i} (I_{sp}(\overline{x}))$	Minimum value in I_{sp}
D_i	$max_i - min_i$	Highest value difference
V_i	$\vert H_i \vert$	Volume (mm^3)
$\overline{G}_i$	$\sum_{\overline{x} \in H_i} \frac{\overline{x} I_{sp}(\overline{x})}{\vert H_i \vert}$	Weighted center of mass
	$(g_1, g_2, g_3) = \overline{G}_i$	
	$(m_1, m_2, m_3) = \overline{m}$	
Δ_i	$\sqrt{\left(\sum_{j=1}^{3} (g_j - m_j)^2 \right)}$	Distance from inj. region
R^A_i	$\frac{V_i}{\vert \{ \overline{x} \in C^{I_{sp}, I_{ct}} \vert I^s_{ct}(\overline{x}) = 1 \} \vert}$	Air ratio
R^F_i	$\frac{V_i}{\vert \{ \overline{x} \in C^{I_{sp}, I_{ct}} \vert I^s_{ct}(\overline{x}) = 2 \} \vert}$	Fat ratio
R^M_i	$\frac{V_i}{\vert \{ \overline{x} \in C^{I_{sp}, I_{ct}} \vert I^s_{ct}(\overline{x}) = 3 \} \vert}$	Muscle ratio
R^B_i	$\frac{V_i}{\vert \{ \overline{x} \in C^{I_{sp}, I_{ct}} \vert I^s_{ct}(\overline{x}) = 4 \} \vert}$	Bone ratio

Where $1 \leq i \leq ID$ represents the i^{th} hot spot. Note that there are indices derived from others, while some are directly derived from the images.

Based on the above definitions, several indices were calculated for all $H_i \in H$ hot spots detailed in Tab. II.

The calculated indices were the base of further classifications. The classification was performed by multiple conditions defined over the derived indices as shown in Tab III. If an i hot spot met all these conditions for all $H_i \in H$, then it was classified as true finding ($i \in HT$) otherwise it was classified as a false one ($i \in HF$). For an example of the above classification see Fig. 3.

4) Validation: Two medical physician experts compared the results of our method to the corresponding medical reports of all patients. The breast and prostate cases were handled separately. The result of our classification method

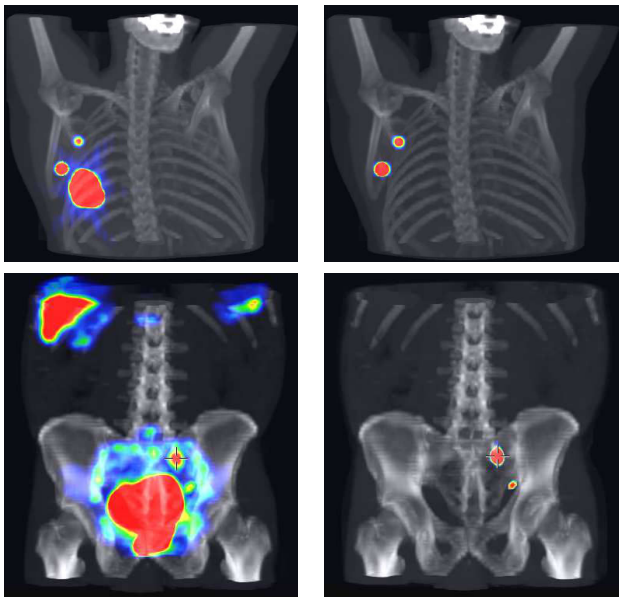

Fig. 3. A fused 3D MIP (Maximum Intensity Projection) view of a breast (top) and a prostate (bottom) SPECT-CT case before (left) and after (right) applying our method.

TABLE III
CONDITIONS TO CLASSIFY HOT SPOTS

Index	Condition
D_i	$> 10Cts$
Δ_i	$< 250mm$
R_i^A	> 0.3
R_i^F	> 0.1
R_i^M	< 0.5
R_i^B	< 0.5

Where $1 \leq i \leq ID$ represents the i^{th} hot spot.

could be changed by the physicians in case of all hot spots. All of these changes were recorded.

For breast cases the number true true-to-false and false-to-true post-classifications were counted in υ_B^+ and υ_B^- values respectively. The total number of the detected hot spots over the breast cases were counted in ϵ_B. The ratio of the false positive and false negative classifications were calculated by $\left(\frac{\upsilon_B^+}{\epsilon_B}\right)$ and $\left(\frac{\upsilon_B^-}{\epsilon_B}\right)$ respectively.

The values υ_P^+, υ_P^- and ϵ_P were consequently calculated for the prostate cases as well.

III. RESULTS

Based on our medical data 3472 and 5354 individual hot spots were detected and classified in breast and prostate cancer cases respectively. For detailed measurements of false positive and false negative ratios see Tab. IV.

TABLE IV
TRUE AND FALSE POSITIVE CLASSIFICATION RATIOS OF OUR METHOD

Type	False positive ratio	False negative ratio
Breast	0.06756	0.00821
Prostate	0.09618	0.02073

IV. CONCLUSIONS AND FUTURE WORKS

A. Conclusions

Based on the achieved low false negative ratio, our method is considered to be a very effective automated solution to support physicians working with lymph node SPECT-CT images. Our false positive ratio is considered to be acceptable as well, since the modification of these cases still requires much less time then the manual processing of a lymph node patient. Average 1 minute was necessary for our method to provide a complete classification on a lymph node image, which is comparable to the average 1 hour time necessary to manually process such a patient.

B. Future Works

As the next step of our research we will focus on the application of neural networks to fine tune the conditions defined in Tab. III. We will also investigate the possibility of fuzzy decision making based on the multiple values of current indices.

REFERENCES

[1] H. Lerman, U. Metser, G. Lievshitz, et al., Lymphoscintigraphic sentinel node identification in patients with breast cancer: the role of SPECT-CT , *Eur J Nucl Med.*, vol. 33, 2006, pp. 329-337.

[2] H. Lerman, G. Lievshitz, O. Zak, et al., Improved Sentinel Node Identification by SPECT/CT in Overweight Patients with Breast Cancer, *J Nucl Med.*, vol. 48, 2007, pp. 201-206.

[3] A. Sherif, U. Garske, M. Torre, et al., Hybrid SPECT-CT: An Additional Technique for Sentinel Node Detection of Patients with Invasive Bladder Cancer, *European Urology*, vol. 50, 2006, pp. 83-91.

[4] A. Martinez, S. Zerdoud, E. Mery, et al., Hybrid imaging by SPECT/CT for sentinel lymph node detection in patients with cancer of the uterine cervix, *Gynecol Oncol.*, vol. 119, 2010, pp. 431-435.

[5] H. Kizu, T. Takayama, M. Fukuda, et al., Fusion of SPECT and Multidetector CT Images for Accurate Localization of Pelvic Sentinel Lymph Nodes in Prostate Cancer Patients, *J Nucl Med Tech.*, vol. 33, 2005, pp. 78-82.

[6] D. B. Husarik, H. C. Steinert, Single-Photon Emission Computed Tomography/Computed Tomographyfor Sentinel Node Mapping in Breast Cancer, *Seminars in Nuclear Meidicne*, vol. 37, 2007, pp. 29-33.

[7] J-Y. Huang, P-F. Kao, Y-S. Chen, Visual Enhancement for Sentinel Lymph Node Mapping in Breast Cancer by Multiple Display Formats of SPECT/CT Images, *2008. International Conference on BioMedical Engineering and Informatics, 2008. BMEI*, 2008, pp. 286 - 289.

[8] Y. Seo, J. Kurhanewicz, B. L. Franc, et al., Improved prostate cancer imaging with SPECT/CT and MRI/MRSI, *IEEE Transactions on Nuclear Science*, vol. 52, 2005, pp. 1316 - 1320.

[9] S. Gorthi, V. Duay, N. Houhou, M. B. Cuadra, et al., Segmentation of Head and Neck Lymph Node Regions for Radiotherapy Planning Using Active Contour-Based Atlas Registration, *IEEE Journal of Selected Topics in Signal Processing*, vol. 3, 2009, pp. 135.

[10] J. H. Moltz, L. Bornemann, J. M. Kuhnigk, Advanced Segmentation Techniques for Lung Nodules, Liver Metastases, and Enlarged Lymph Nodes in CT Scans, *IEEE Journal of Selected Topics in Signal Processing*, vol. 3, 2009, pp. 122.

[11] T. M. Lehmann, C. Gonner, K. Spitzer, Addendum: B-spline interpolation in medical image processing, *IEEE Transactions on Medical Imaging*, vol. 20, 2001, pp. 660-665.

[12] E. C. Beckmann, Godfrey Newbold Hounsfield, *Physics Today*, vol. 58, pp. 8485.

[13] N. Jamil, T. N. T. Sembok,Z. A. Bakar, Noise removal and enhancement of binary images using morphological operations, *International Symposium on Information Technology, 2008. ITSim*, 2008, pp. 1-6.